The Astrophysical Journal Letters, 922:L29 (7pp), 2021 December 1 https://doi.org/10.3847/2041-8213/ac390d

© 2021. The Author(s). Published by the American Astronomical Society.

OPEN ACCESS

Massive Molecular Outflow and 100 kpc Extended Cold Halo Gas in the Enormous Lyα Nebula of QSO 1228+3128

Jianrui Li[1], Bjorn H. C. Emonts[2], Zheng Cai[1,7,8], J. Xavier Prochaska[5,6], Ilsang Yoon[2], Matthew D. Lehnert[4], Shiwu Zhang[1], Yunjing Wu[1], Jianan Li[1], Mingyu Li[1], Mark Lacy[2], and Montserrat Villar-Martín[3]

[1] Department of Astronomy, Tsinghua University, Beijing, People's Republic of China; zcai@mail.tsinghua.edu.cn
[2] National Radio Astronomy Observatory, 520 Edgemont Road, Charlottesville, VA 22903, USA
[3] Centro de Astrobiologıa (CSIC/INTA), Instituto Nacional de Técnica Aeroespacial, l Ctra de Torrejón a Ajalvir, km 4, E-28850 Torrejón de Ardoz (Madrid), Spain
[4] Université Lyon 1, ENS de Lyon, CNRS UMR5574, Centre de Recherche Astrophysique de Lyon, F-69230 Saint-Genis-Laval, France
[5] UCO/Lick Observatory, University of California, 1156 High Street, Santa Cruz, CA 95064, USA
[6] Kavli Institute for the Physics and Mathematics of the Universe (WPI), The University of Tokyo, Kashiwa 277-8583, Japan
[7] Center for Astronomy Technology, Tsinghua University, Beijing, People's Republic of China
[8] Peng Cheng Laboratory, Shenzhen, People's Republic of China

Received 2021 August 29; revised 2021 October 28; accepted 2021 November 9; published 2021 November 25

Abstract

The link between the circumgalactic medium (CGM) and the stellar growth of massive galaxies at high-z depends on the properties of the widespread cold molecular gas. As part of the SUPERCOLD-CGM survey (Survey of Protocluster ELANe Revealing CO/[C I] in the Lyα-Detected CGM), we present the radio-loud QSO Q1228+3128 at $z = 2.2218$, which is embedded in an enormous Lyα nebula. ALMA+ACA observations of CO(4–3) reveal both a massive molecular outflow, and a more extended molecular gas reservoir across ∼100 kpc in the CGM, each containing a mass of $M_{\rm H2} \sim 4\text{–}5 \times 10^{10}\ M_\odot$. The outflow and molecular CGM are aligned spatially, along the direction of an inner radio jet. After reanalysis of Lyα data of Q1228+3128 from the Keck Cosmic Web Imager, we found that the velocity of the extended CO agrees with the redshift derived from the Lyα nebula and the bulk velocity of the massive outflow. We propose a scenario where the radio source in Q1228+3128 is driving the molecular outflow and perhaps also enriching or cooling the CGM. In addition, we found that the extended CO emission is nearly perpendicular to the extended Lyα nebula spatially, indicating that the two gas phases are not well mixed, and possibly even represent different phenomena (e.g., outflow versus infall). Our results provide crucial evidence in support of predicted baryonic recycling processes that drive the early evolution of massive galaxies.

Unified Astronomy Thesaurus concepts: CO line emission (262); Circumgalactic medium (1879); High-redshift galaxies (734); Galaxy evolution (594)

1. Introduction

At high redshifts, large reservoirs of circumgalactic medium (CGM) are known to play a crucial role in the evolution of massive galaxies. Giant gaseous halos, generally detected in Lyα ($T > 10^4$K), have been known to be associated with massive galaxies in high-z protoclusters since the early 2000s (e.g., Reuland et al. 2003; Villar-Martín et al. 2003; Miley et al. 2006; Cai et al. 2017, 2018). Nevertheless, a limitation in our understanding of the multiphase CGM around distant galaxies is that we have little information about the coldest phase of the CGM. This means that a direct connection to the stellar growth of massive galaxies remains missing, until we identify the ultimate reservoir of halo gas that can fuel widespread star formation, namely the cold molecular gas (∼10–100 K).

This gap in our understanding started to be filled when large amounts of widespread, cold molecular gas were detected in CO, [C I], and [C II] on scales of many tens of kiloparsecs in the halo environments of massive high-z galaxies (e.g., Emonts et al. 2014, 2015, 2016, 2018; Cicone et al. 2015, 2021; Ginolfi et al. 2017; Frayer et al. 2018; Fujimoto et al. 2019). The best studied example is the Spiderweb Galaxy, which contains a giant (∼250 kpc) Lyα halo (Miley et al. 2006). Sensitive surface-brightness observations of CO(1–0), CO(4–3), and [C I] $^3P_1$-$^3P_0$ revealed a widespread (∼70 kpc) reservoir of cold molecular gas across the CGM of the Spiderweb (Emonts et al. 2016, 2018). This cold CGM has a carbon abundance and excitation properties similar to the ISM in star-forming galaxies (Emonts et al. 2018), and follows diffuse blue light from in situ star formation in the CGM (Hatch et al. 2008; Emonts et al. 2016). This suggests that recycling and mixing through metal-enriched outflows or mass transfer among galaxies, as well as star formation, occurs on a massive scale in the CGM of the Spiderweb (Narayanan et al. 2015; Faucher-Giguère et al. 2016). Recently, molecular gas on even larger scales was detected in CO(3–2) across the CGM around a quasar at $z \sim 2$ (Cicone et al. 2021). If other high-z protocluster galaxies show similar nebulae with cold star-forming gas, then this requires us to revise our ideas of star formation, and the early build-up of the most massive galaxies in the universe.

Driven by the major advances in optical integral-field-unit (IFU) spectrographs, a new sample of giant Lyα-emitting nebulae reminiscent of the Spiderweb, and sufficiently luminous for quantitative analysis of diffuse gas emission, was discovered. These "Enormous Lyα Nebulae (ELANe)" are the extrema of Lyα nebulae at $z \sim 2$–3, with sizes exceeding the diameters of even massive dark matter halos (∼250 kpc) and Lyα luminosities $>10^{44}$ erg s^{-1} (Cantalupo et al. 2014; Hennawi et al. 2015; Borisova et al. 2016; Cai et al. 2017;

Original content from this work may be used under the terms of the Creative Commons Attribution 4.0 licence. Any further distribution of this work must maintain attribution to the author(s) and the title of the work, journal citation and DOI.

Arrigoni Battaia et al. 2019). They generally contain one or more luminous AGN, and are typically located within protoclusters. To trace the molecular CGM across ELANe, the Karl G. Jansky Very Large Array (VLA) was used to observe the enigmatic Mammoth ELAN (Emonts et al. 2019). These data reveal a large reservoir of cold molecular gas ($\sim 6 \times 10^{10}\,M_{\odot}$) that is spread across tens of kiloparsecs in the CGM, even in the presence of an obscured quasi-stellar object (QSO). This suggests that a molecular CGM may occur among the general population of ELANe. However, in other ELANe, such a molecular CGM was not detected (Decarli et al. 2021).

To study the CGM around active galaxies in the early universe in a systematic way, we started a survey with the Atacama Large Millimeter/submillimeter Array (ALMA), ALMA Compact Array (ACA), and Karl G. Jansky VLA entitled SUPERCOLD-CGM: "Survey of Protocluster ELANe Revealing CO/CI in the Lyα Detected CGM." The goal of the SUPERCOLD-CGM survey is to use radio telescopes with short baseline configurations to image low-surface-brightness CO and [C I] emission of widespread cold molecular gas around the massive host galaxies of active galactic nuclei (AGNs) at high-z. Our initial ALMA/ACA sample consists of 10 type-I QSOs at $z \sim 2$, which were selected from the SDSS-IV/eBOSS sample (e.g., Pâris et al. 2017). These QSOs contain ELANe mapped by the Keck Cosmic Web Imager (KCWI; Cai et al. 2019). Here we present observations sensitive to low-surface-brightness emission of molecular gas, CO(4–3), of Q1228+3128 at $z = 2.2218$. Q1228+3128 is the most extended and brightest Lyα nebula in our sample of ELANe. We assume a ΛCDM cosmology with $H_0 = 70$ km s^{-1} Mpc^{-1}, $\Omega_M = 0.30$, and $\Omega_\Lambda = 0.70$, i.e., 8.25 kpc/$''$ and $D_L = 17620$ Mpc at $z = 2.2218$.

2. Observation and Data Reduction

We observed Q1228+3128 (12:28:24.97, 31:28:37.70) at $z = 2.2218$ for 1.5 hr on-source during ALMA cycle-7 on 2019 November 20 and 23 and 2020 January 4 with a compact configuration (C43-2) of the 12 m Array (51 antennas), which baselines range from 15 to 314 m, as well as for 12.4 hr between 2019 October ~ 2020 March with the ACA 7 m Array (12 antennas). We simultaneously centered two adjacent spectral windows of 1.875 GHz on CO(4–3) at $\nu_{\rm obs} \sim 143.10$ GHz ($\nu_{\rm rest} = 461.04$ GHz) and another two spectral windows to cover the continuum but also including part of the [C I] ^{3}P$_1$-^{3}P$_0$ line, which is also detected but much weaker and fell at the outer edge of the band. The [C I] results will be discussed in a future paper.

The ALMA data were reduced in CASA 5.6.1-8 (Common Astronomy Software Applications; McMullin et al. 2007). To calibrate the data, we used the archival calibration script supplied by ALMA. After the calibration, we subtracted the continuum from the data by fitting a straight line to the line-free channels in the UV-domain, and then combined the respective 12 m and 7 m data sets in preparation for imaging in tclean.[9] In the step of tclean, we imaged the 12 m data using natural weighting, and also imaged the combined 12 m + 7 m data sets using various degrees of tapering.[10] In this paper, we present the combined 12 m + 7 m data tapered to the baseline of 39 m. We also present the untapered (full-resolution) data derived from the continuum-subtracted 12 m Array. In addition, we obtained multifrequency synthesis images of the 150 GHz rest-frame continuum by imaging the line-free channels of the 12 m and 7 m data using natural weighting, which revealed an unresolved point source with flux density $S_{150\,\rm GHz} = 8.1 \pm 0.5$ mJy beam^{-1}.

For the tapered and untapered CO(4–3) line-data sets, we imaged our field out to ~70$''$ and binned both of them to 60 km s^{-1} per channel. We then convolved the tapered CO(4–3) data cube with a 5$''$.0 × 5$''$.0 Gaussian to obtain a smoothed synthesized beam of 8$''$.0 × 7$''$.5 with PA = 24°.2. The synthesized beam size of the untapered CO(4–3) data cube is 2$''$.8 × 2$''$.0 with PA = 13°.6. The rms noise of the untapered and smoothed tapered CO(4–3) data cubes is 0.17 and 0.32 mJy beam^{-1} channel^{-1}, respectively. To get position–velocity (P-V) maps, we binned our smoothed tapered CO(4–3) datacube to 180 km s^{-1} per channel, resulting in a noise of 0.18 mJy beam^{-1} channel^{-1}.

To check the validity of the features that we describe in this paper, we also performed a self-calibration using the model of the continuum image. All features that we describe in this paper were still present in the self-calibrated data cubes. However, since the continuum is faint, our data quality did not improve after the self-calibration. Therefore we present in this paper the data products without self-calibration applied. Also, we found that the flux density of the 12 m and 7 m data was consistent when comparing the continuum image of the unresolved radio continuum in the untapered 12 m data and the smoothed tapered 12 m + 7 m data, which confirmed that the flux calibration between the different data sets is accurate.

3. Results

The left panel of Figure 1 shows the total intensity map of CO(4–3) collapsed from the smoothed tapered data cube integrated within the velocity range of $-596 < v < -236$ km s^{-1}, and the right panel shows the position–velocity (P-V) map extracted along the P-V slice-direction indicated in the left panel. Both of them revealed a very extended reservoir of CO, which is spreading more than 100 kpc in NE direction. "Q" and "E" resemble the QSO and the extended region, respectively.

The left panel of Figure 2 shows the 1D spectrum extracted from the smoothed tapered CO(4–3) data cube against the peak of the CO emission associated with the quasar. To measure the quasar centroid, we collapsed a total intensity broadband map integrated within the velocity range of -1217 km s^{-1} $< v < 883$ km s^{-1} from the untapered data cube and then regard the brightest pixel in CO as the QSO centroid. This is also consistent with the optical coordinate of the QSO. The spectrum was fitted by a double Gaussian, a narrow component to fit the central core, tracing the quiescent gas in the QSO, and a broad component to fit the broad wings. The curve fit Python package[11] was used to do this fitting. We chose the area, center,

---

[9] https://casadocs.readthedocs.io/en/stable/api/tt/casatasks.imaging.tclean.html

[10] Tapering means applying a Gaussian taper to the weights of the UV-data during imaging, which increases the weighting of the shorter baselines. This decreases spatial resolution and increases the surface-brightness sensitivity for detecting extended emission.

[11] https://docs.scipy.org/doc/scipy-0.15.1/reference/generated/scipy.optimize.curve_fit.html

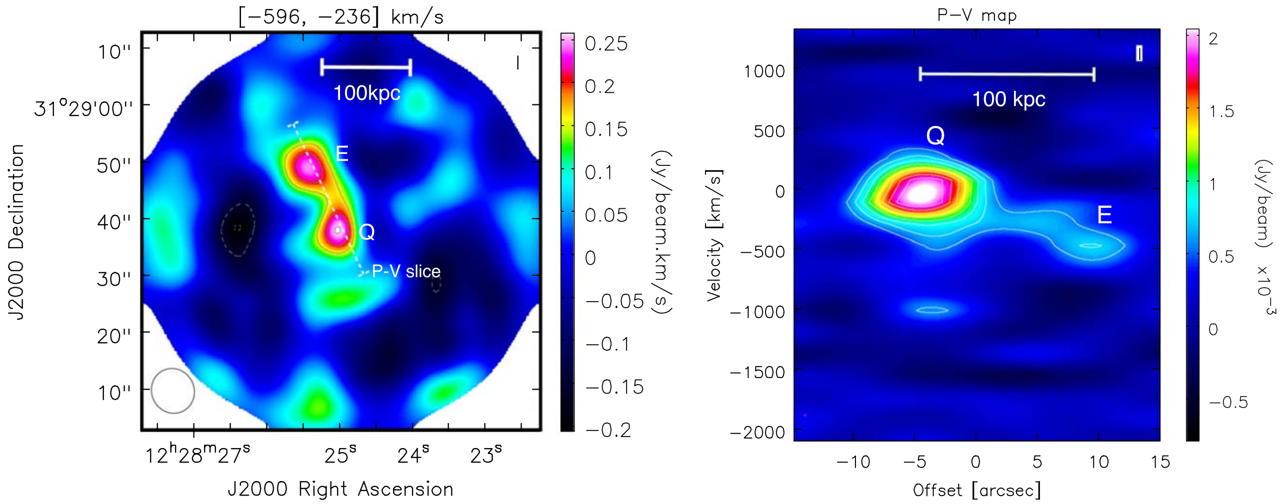

Figure 1. Left: total intensity map collapsed from the smoothed tapered CO(4–3) data cube integrated within $(-596 < v < -236)$ km s^{-1} and 1σ is 0.05 Jy beam^{-1} km s^{-1}. Right: position–velocity (P-V) map extracted along the P-V slice-direction indicated in the above panel with 1σ equaling 0.18 mJy beam^{-1} channel^{-1}. In both panels, contours start at 3σ and increase with 1σ.

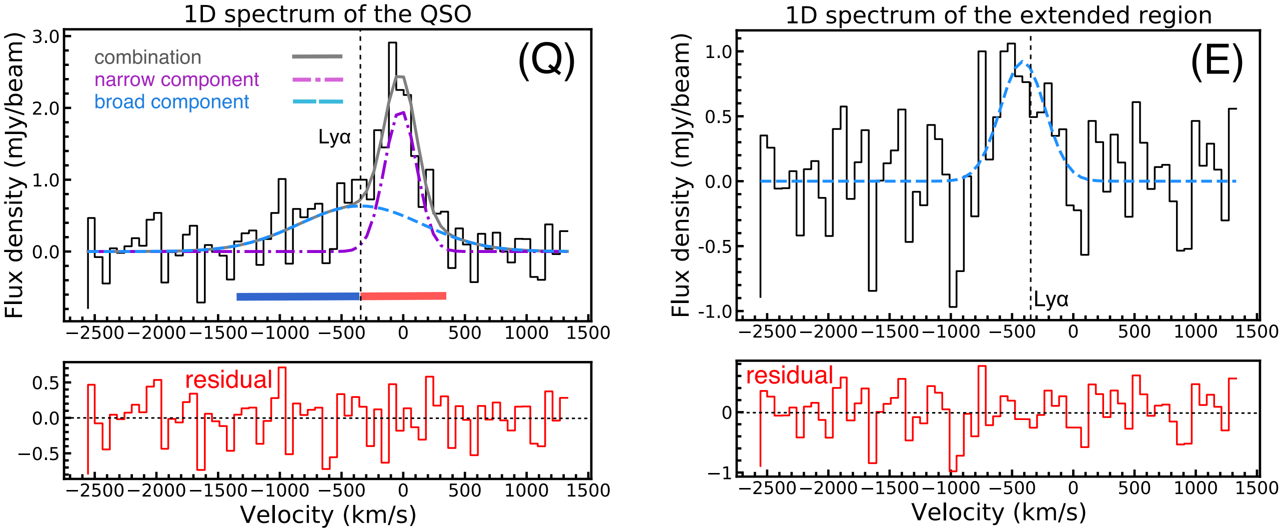

Figure 2. Left: 1D spectrum of the beam-integrated CO(4–3) flux extracted from the smoothed tapered data cube against the peak of the CO emission associated with the quasar. A double Gaussian fit has been applied to the line profile (black), including a narrow systemic component that traces quiescent gas and a broad blueshifted line component that traces the outflow. The gray line shows the combination of the two Gaussian functions and the red spectrum in the bottom panel shows the residual. The vertical dashed black line shows the mean redshift of diffuse Lyα emission in CO(4–3) frame (the same as the right panel). Right: 1D spectrum of the beam-integrated CO(4–3) flux extracted from the smoothed tapered data cube after primary beam correction against the peak of the CO emission in the extended region. Also, a Gaussian fit (dashed blue line) has been applied to the line profile (black), and the red spectrum shows the residual.

Table 1
Results of the Gaussian Fits to the CO(4–3) Emission Line Spectrum of the QSO and Extended Region

Component	v (km s^{-1})	σ_v (km s^{-1})	I_ν (Jy km s^{-1})	$L'_{\mathrm{CO(4--3)}}$ (10^{10} K km s^{-1} pc^2)	$M_{\mathrm{H_2}}$ 10^{10} $M_\odot$
Narrow	-21 ± 17	130 ± 20	0.64 ± 0.13	0.94 ± 0.19	3.4 ± 0.7
Broad	-346 ± 130	495 ± 96	0.79 ± 0.18	1.17 ± 0.26	4.2 ± 0.9
Extended emission	-413 ± 45	182 ± 44	0.43 ± 0.09	0.62 ± 0.13	5.0 ± 1.0

and sigma in the Gaussian function as free parameters, and regarded the 1/rms of each channel as the weighting. The broad component in Figure 2 (left) has a full width at half-maximum intensity of FWHM = 1160 km s^{-1}, which is significantly larger than what is typically for high-z QSOs and submillimeter galaxies (Carilli & Walter 2013). We therefore argue that this broad component is most likely a massive outflow of molecular gas. The right panel of Figure 2 shows the 1D spectrum extracted against the peak of the CO(4–3) emission in the extended region from the smoothed tapered data cube after primary beam correction. The spectrum was fitted by a Gaussian function (dashed blue line) in the same way described above. The fitting results and the corresponding luminosity and gas mass are reported in Table 1. Figure 6 in Appendix B shows an analysis of the extended CO emission in the UV-domain by plotting the UV distance of the baselines

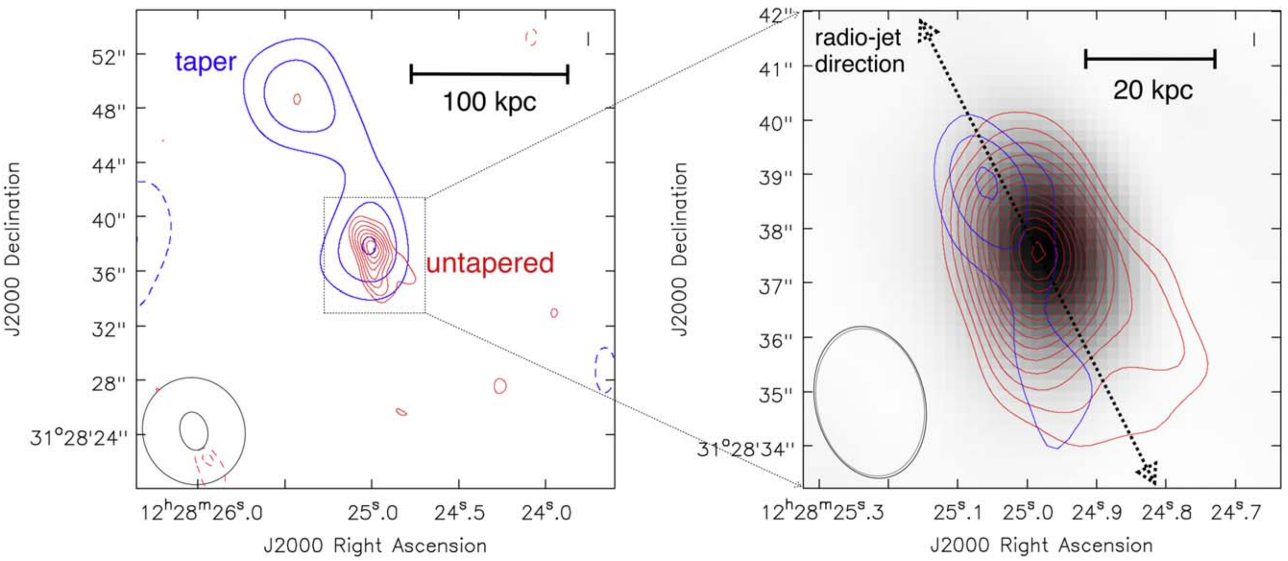

Figure 3. Left: the blue contours show the total intensity CO(4–3) map from Figure 1. The red contours show the total intensity map collapsed from the untapered CO(4–3) data cube integrated within $v \in (-1217, 883)$ km s^{-1} and 1σ is 0.097 Jy beam^{-1} km s^{-1}. The synthesized beams of the tapered and untapered data are shown in the bottom left corner of this panel. Right: the blue and red contours are the total intensity contour map collapsed from the untapered CO(4–3) data cube integrated within $v \in (-1217, -377)$ km s^{-1} and $v \in (-377, 343)$ km s^{-1} with 1σ equal to 0.046 and 0.047 Jy beam^{-1} km s^{-1}, respectively. The velocity ranges across which we integrated the systemic and outflow signal are indicated with red and blue bars in the quasar spectrum in Figure 2. The background shows the ALMA continuum image. In both panels, contours start at 3σ and increase with 1σ. The black dashed arrow represents the radio-jet direction (Helmboldt et al. 2007).

against the real part of the visibility amplitudes in the extended region (Ivison et al. 2010; Cicone et al. 2021). With the length of baselines decreasing, the flux increases conspicuously. From the Gaussian fitting (dashed red line in Figure 6), we derived an FWHM = ($8''.8 \pm 1''.7$) of the extended CO emission in the image plane, which corresponds to a minimum spatial extent of 73 ± 14 kpc. The zero-baseline flux is 1.03 ± 0.25 mJy, which is consistent with the right panel of Figure 2.

To estimate molecular gas masses, for the QSO, as thermal excitation is reasonable, we assume $r_{4-3/1-0} = L'_{\mathrm{CO(4-3)}}/L'_{\mathrm{CO(1-0)}} = 1$ (Riechers et al. 2011) and for the extended emission we assume $r_{4-3/1-0} = L'_{\mathrm{CO(4-3)}}/L'_{\mathrm{CO(1-0)}} = 0.45$ (Emonts et al. 2018). The molecular gas mass $M_{\mathrm{H_2}}$ is derived from $L'_{\mathrm{CO(1-0)}}$ (Solomon & Vanden Bout 2005), assuming $\alpha_{\mathrm{CO}} = 3.6\, M_\odot$ (K km s^{-1} pc^2)$^{-1}$ (Daddi et al. 2010; Genzel et al. 2010; Bolatto et al. 2013). In this case, the molecular gas mass $M_{\mathrm{H_2}}$ of the QSO host galaxy, outflow, and extended region that we derived from the smoothed tapered data cube is (3.4 ± 0.7), (4.2 ± 0.9), and $(5.0 \pm 1.0) \times 10^{10}$ $M_\odot$, respectively.

The left panel of Figure 3 shows the extended emission at two different resolutions. The red contours represent the total intensity map collapsed from all the line emission channels of the full-resolution (untapered) CO(4–3) data cube, which is spread across ∼25 kpc. The blue contours represent the total intensity map collapsed from the blue side of $-596 < v < -236$ km s^{-1} of the smoothed tapered data cube, revealing emission on scales of more than 100 kpc. The right panel of Figure 3 shows the two components of the untapered CO(4–3) data cube separated spatially. The red and blue contours represent the quiescent gas in the QSO host galaxy and the blue-sided outflow, respectively. There is an offset of ∼15 kpc between the central QSO component and the peak of the CO emission in the outflow. We can make a rough estimate of the mass flow rate of the outflow if we assume that the outflow originated from the QSO core and traveled at a velocity of Δv + 0.5 × ($\mathrm{FWHM_{outflow}}$), with Δv the velocity difference between the peak velocity of the narrow and broad component and FWHM = $2.35\sigma_v$ (Table 1). This results in an estimated outflow rate of $\dot{M}_{\mathrm{H2}} \sim 2600\, M_\odot$ yr^{-1}. The background in Figure 3 shows the ALMA continuum image and the dashed black arrow represents the radio-jet direction (Helmboldt et al. 2007), which is the same as the outflow direction.

The left panel of Figure 4 shows an optimally reextracted image from PSF- and continuum-subtracted data previously obtained with the KCWI of the Lyα nebula around Q1228+3128 (see Cai et al. 2019). And the right panel of Figure 4 shows the kinematics image of the Lyα nebula in our CO(4–3) frame, with "0 km s^{-1}" corresponding to $z = 2.2218$, determined from the narrow component of CO(4–3).

4. Discussion

We have presented large-scale extended CO(4–3) emission spread across ∼100 kpc and a massive blue-sided outflow from QSO 1228+3128 at $z = 2.2218$ as part of the SUPERCOLD-CGM survey. For the central outflow, there is an offset of 15 kpc between the peak of the systemic CO emission in the host galaxy and the CO in the outflow component, with the outflow found toward the NE (see the right panel of Figure 3). The much more extended and quiescent CO reservoir, found after tapering and smoothing our data, stretches across 100 kpc in the same direction as the central outflow, and has roughly the same velocity as the bulk velocity of the outflow (see Figure 2). This demonstrates that the molecular outflow and the extended, quiescent molecular gas reservoir may have the same origin. After reanalysis of Lyα data of Q1228+3128 from the KCWI, we converted the Lyα emission into our CO(4–3) redshift frame and found that the mean redshift of the Lyα nebula is close to −350 km s^{-1}, which is very consistent with the bulk velocity of the outflow and extended CO reservoir.

Our case of Q1228+3128 resembles the detection by Cicone et al. (2015) of a massive outflow of [C II] and a very extended [C II] reservoir from the radio-quiet QSO host galaxy SDSS

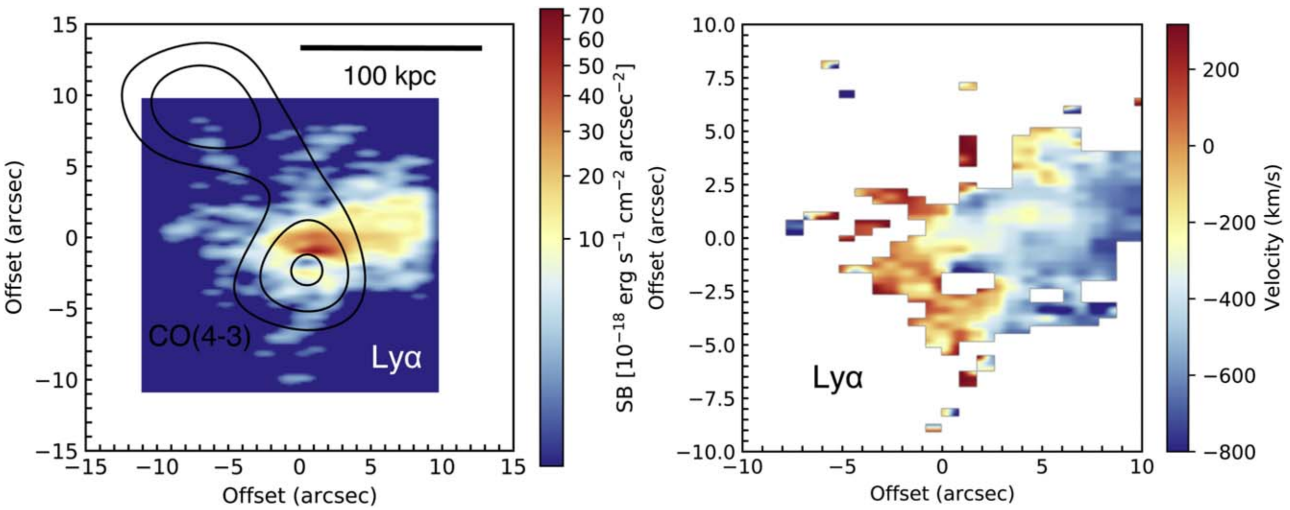

Figure 4. Left: the black contours show the total intensity CO(4–3) map from Figure 1, and the background shows the "optimally extracted" Lyα nebula image from PSF- and continuum-subtracted KCWI data cubes for Q1228+3128 starting at 2σ, which corresponds to 1.9×10^{-18} erg s^{-1} cm^{-2} arcsec^{-2}. Right: the kinematics image of the Lyα nebula shown on the left side, with "0 km s^{-1}" corresponding to $z = 2.2218$.

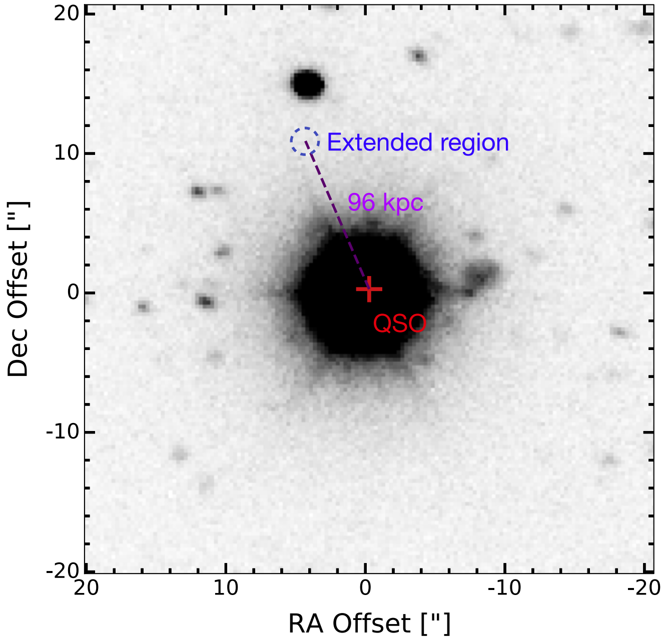

Figure 5. The deep optical image of Q1228 from the Low Resolution Imaging Spectrometer (LRIS) of Keck. The blue side G filter covering 416.173 ∼ 524.362 nm was chosen for imaging. The small dashed blue circle shows the photometry aperture of the extended region, and the red cross shows the QSO.

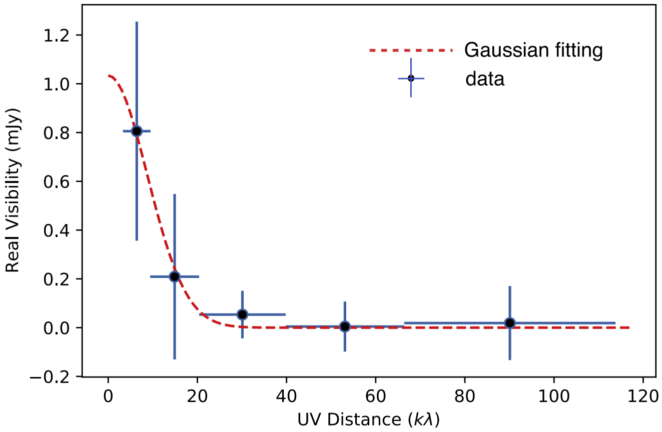

Figure 6. UV plot of the 12 m and 7 m ACA combined CO(4–3) data in the extended region. The vertical and horizontal blue bars represent the error of the flux and the UV distance range per bin respectively. The dashed red line shows the fit of a model of a Gaussian distribution with a flux = 1.03 ± 0.25 mJy and an FWHM = (8.8 ± 1.7)″.

J1148+5251 at $z > 6$, with filamentary structures that have a complex morphology and reach a maximum projected radius of ∼30 kpc. They found quasar feedback is likely the dominant mechanism driving the outflow, and their observations are qualitatively consistent with radiation-pressure driven dusty shells. Compared to SDSS J1148+5251, the molecular outflow and quiescent CO reservoir appear to be much more collimated in Q1228+3128.

We know from existing radio data from FIRST (Faint Images of the Radio Sky at Twenty-Centimeters; Becker et al. 1994) and VLASS (VLA Sky Survey; Lacy et al. 2020) that Q1228+3128 is the only radio-detected QSO, or quasar, in our 10 target sample. In addition, as a flat-spectrum radio source, it was shown by Helmboldt et al. (2007) that there is a radio jet at a scale of a few tens of milliarcsec in the same direction as our extended CO reservoir and massive outflow (see Figure 3). In high-z radio galaxies (HzRGs), the CO emission is often aligned with the radio-jets and found tens of kiloparsecs outside the host galaxy (Klamer et al. 2004; Emonts et al. 2014; Falkendal et al. 2021). The most intriguing part of our work is that Q1228+3128 is the first radio source at high-z where both phenomena have been observed simultaneously.

For our target, the outflow and extended CO reservoir have roughly the same bulk velocity (see Table 1), and are both aligned in the same direction. We propose the scenario that the extended CO-emitting gas is formed when the propagating radio jet drives the outflow, shocks, and cools preexisting dusty halo gas (Emonts et al. 2016; Gullberg et al. 2016), and possibly also enriches the gas by dragging metals out into the environment (Kirkpatrick et al. 2011). If this scenario is viable, we can make the testable prediction that a faint extended radio jet should be found to be aligned with the extended CO(4–3) emission with sensitive surface-brightness (low resolution but high sensitivity on short baselines) radio imaging.

The diffuse Lyα nebula also owns the same mean velocity as the extended CO reservoir. However, because the spatial distribution of the extended CO and Lyα emission appears to be almost perpendicular, the respective cold and warm gas phases may not represent a well-mixed CGM. Villar-Martín et al. (2003) kinematically resolved the emission from ambient nonshocked gas (the quiescent halos) and the emission from (jet-induced) shocked gas of a sample of 10 high-redshift radio galaxies at $z \sim 2.5$. They argue that the quasar continuum is the dominant excitation mechanism of the quiescent halos along the radio axis. In our case, if the radio jet is responsible for the cooling and enrichment of gas in the CGM, then photoionization of the quasar would be expected to occur roughly along the same direction, which would not explain the perpendicular orientation of the extended CO and Lyα emission. Instead, an alternative scenario is that the Lyα emission may be infalling gas behind the quasar. It is widely recognized that the collisions with cold gas streams could excite Lyα emission (Dijkstra & Loeb 2009; Goerdt et al. 2010; Rosdahl & Blaizot 2012; Vernet et al. 2017). Observationally, Daddi et al. (2021) performed imaging of the Lyα kinematics across a 300 kpc-wide giant Lyα nebula centered on the massive galaxy group RO-1001, which contains three Lyα-emitting filaments and may indicate the case for gas infall. An inflow of gas was also proposed by Vernet et al. (2017) to describe the Lyα properties of MRC 0316-257 at $z \sim 3$. The Lyα nebula of Q1228+3128 could present a similar case.

Another alternative scenario is that there is a separate merging galaxy in the extended region, and that the extended molecular gas is tidal debris from galaxy interactions. Although we see a 3σ detection of the extended region in the untapered CO(4–3) image, the total flux of the extended region in the untapered CO(4–3) image is only $\sim$40% of that in the smoothed tapered image, meaning that the bulk of the extended emission is spread on scales that are over-resolved even with the compact 12 m ALMA array (see Figure 6). If there is a companion galaxy associated with part of the CO(4–3) emission, it is associated with a nondetection in the ALMA continuum image. When converting the 3σ flux density of 0.15 mJy from the untapered continuum image to the IR luminosity ($L_{\mathrm{IR\_SF}}$) integrated within the wavelength range $8 \sim 1000\ \mu$m, we derived an upper limit for the L_{IR}, which is $3.0 \times 10^{12}\ L_\odot$ (Wang et al. 2008). According to the correlation between $L'_{\mathrm{CO(4-3)}}$ and L_{IR} described in Greve et al. (2014), we derived a L_{IR} of the extended region that is $(4.5 \pm 1.0) \times 10^{11}\ L_\odot$ from untapered $L'_{\mathrm{CO(4-3)}}$. The fact that the L_{IR} limit for detecting the continuum is much higher than that calculated for CO(4–3) means we do not have the sensitivity at this frequency to detect the continuum. However, a deep optical image of Q1228 obtained with Keck (see Appendix A) helped us to investigate the existence of the companion galaxy. Although the QSO was saturated, there is still a nondetection in the extended region. Using the 3σ flux density of 3.0×10^{-30} erg s^{-1} cm^{-2} Hz^{-1}($g_{\mathrm{AB}} \sim 25$ mags) from an aperture with diameter equating $2''$, we derived an upper limit of the star formation rate (SFR) for the extended region from the deep optical image, which is $2.4\ M_\odot$ yr^{-1} (Kroupa 2001). But the $L'_{\mathrm{CO(4-3)}}$ predicts an SFR of $49 \pm 12\ M_\odot$ yr^{-1} (Kennicutt 1998), which is much higher than the optical result. This, combined with the fact that the total amount of molecular gas that must be spread on large scales as part of the tidal debris would be comparatively large ($\sim 3 \times 10^{10}\ M_\odot$), suggests that the extended emission is not likely the result of a tidal interaction with a companion galaxy.

Z.C. and J.L. are supported by the National Key R&D Program of China (grant No. 2018YFA0404503), the National Science Foundation of China (grant No. 12073014), and Tsinghua University Initiative Scientific Research Program (grant No. 2019Z07L02017). MVM work was funded by grant PGC2018-094671-B-I00, MCIN/AEI/10.13039/501100011033, and by the European Union NextGenerationEU PRTR. We thank the anonymous referee for the very valuable feedback. This paper makes use of the following ALMA data: ADS/JAO.ALMA#2019.1.01251.S. ALMA is a partnership of ESO (representing its member states), NSF (USA) and NINS (Japan), together with NRC (Canada), MOST and ASIAA (China, Taiwan), and KASI (Republic of Korea), in cooperation with the Republic of Chile. The Joint ALMA Observatory is operated by ESO, AUI/NRAO and NAOJ. The National Radio Astronomy Observatory is a facility of the National Science Foundation operated under cooperative agreement by Associated Universities, Inc.

Appendix A
Deep Optical Image of Q1228

Figure 5 shows the deep optical image of Q1228 from the Low Resolution Imaging Spectrometer (LRIS) of Keck. The observation was done on 2021 July 8 with a total on-source time of 25 minutes. The blue side G filter covering $416.173 \sim 524.362$ nm was chosen for imaging. We first reduced the data in lpipe and then used the SEXTRACTOR, SCAMP, and SWARP to do the calibration of WSC and the final stacking process.

Appendix B
A Radial UV Plot of the Extended Region

Figure 6 shows the UV distance plotted against the real part of the visibility amplitude of the CO(4–3) emission in the extended region. In order to obtain this plot, we first split out the combined 12 m + 7 m data sets to only contain the channel range ($143.17 \sim 143.40$ GHz) corresponding to the extended emission, and then shifted the phase center from the QSO to the extended region (ICRS: 12:28:25.427, 31.28.48.975). We then extracted all the data points and binned them. Finally, we fitted the Fourier transform of a Gaussian function to the data points, which corresponds to the model of a Gaussian distribution in the image plane.

ORCID iDs

Jianrui Li https://orcid.org/0000-0003-0994-1512
Bjorn H. C. Emonts https://orcid.org/0000-0003-2983-815X
Zheng Cai https://orcid.org/0000-0001-8467-6478
J. Xavier Prochaska https://orcid.org/0000-0002-7738-6875
Ilsang Yoon https://orcid.org/0000-0001-9163-0064
Matthew D. Lehnert https://orcid.org/0000-0003-1939-5885
Yunjing Wu https://orcid.org/0000-0003-0111-8249
Mark Lacy https://orcid.org/0000-0002-3032-1783

References

Arrigoni Battaia, F., Hennawi, J. F., Prochaska, J. X., et al. 2019, MNRAS, 482, 3162
Becker, R. H., White, R. L., Helfand, D. J., Greeg, M. D., & Perley, R. A. 1994, BAAS, 26, 1317
Bolatto, A. D., Wolfire, M., & Leroy, A. K. 2013, ARA&A, 51, 207
Borisova, E., Cantalupo, S., Lilly, S. J., et al. 2016, ApJ, 831, 39
Cai, Z., Fan, X., Yang, Y., et al. 2017, ApJ, 837, 71
Cai, Z., Fan, X., Bian, F., et al. 2017, ApJ, 839, 131
Cai, Z., Hamden, E., Matuszewski, M., et al. 2018, ApJL, 861, L3
Cai, Z., Cantalupo, S., Prochaska, J. X., et al. 2019, ApJS, 245, 23
Carilli, C. L., & Walter, F. 2013, ARA&A, 51, 105
Cicone, C., Maiolino, R., Gallerani, S., et al. 2015, A&A, 574, A14
Cicone, C., Mainieri, V., Circosta, C., et al. 2021, A&A, 654, L8
Cantalupo, S., Arrigoni-Battaia, F., Prochaska, J. X., et al. 2014, Natur, 506, 63
Daddi, E., Valentino, F., Rich, R. M., et al. 2021, A&A, 649, A78
Daddi, E., Bournaud, F., Walter, F., et al. 2010, ApJ, 713, 686
Decarli, R., Arrigoni-Battaia, F., Hennawi, J. F., et al. 2021, A&A, 645, L3
Dijkstra, M., & Loeb, A. 2009, MNRAS, 400, 1109
Emonts, B. H. C., Norris, R. P., Feain, I., et al. 2014, MNRAS, 438, 2898
Emonts, B. H. C., Mao, M. Y., Stroe, A., et al. 2015, MNRAS, 451, 1025
Emonts, B. H. C., Lehnert, M. D., Villar-Martín, M., et al. 2016, Sci, 354, 1128
Emonts, B. H. C., Lehnert, M. D., Dannerbauer, H., et al. 2018, MNRAS, 477, L60
Emonts, B. H. C., Cai, Z., Prochaska, J. X., et al. 2019, ApJ, 887, 86
Falkendal, T., Lehnert, M. D., Vernet, J., et al. 2021, A&A, 645, A120
Faucher-Giguère, C.-A., Feldmann, R., Quataert, E., et al. 2016, MNRAS, 461, L32
Frayer, D. T., Maddalena, R. J., Ivison, R. J., et al. 2018, ApJ, 860, 87
Fujimoto, S., Ouchi, M., Ferrara, A., et al. 2019, ApJ, 887, 107
Genzel, R., Eisenhauer, F., & Gillessen, S. 2010, RvMP, 82, 3121
Ginolfi, M., Maiolino, R., Nagao, T., et al. 2017, MNRAS, 468, 3468
Goerdt, T., Dekel, A., Sternberg, A., et al. 2010, MNRAS, 407, 613
Greve, T. R., Leonidaki, I., Xilouris, E. M., et al. 2014, ApJ, 794, 142
Gullberg, B., Lehnert, M. D., De Breuck, C., et al. 2016, A&A, 591, A73
Hatch, N. A., Overzier, R. A., Röttgering, H. J. A., et al. 2008, MNRAS, 383, 931
Helmboldt, J. F., Taylor, G. B., Tremblay, S., et al. 2007, ApJ, 658, 203
Hennawi, J. F., Prochaska, J. X., Cantalupo, S., et al. 2015, Sci, 348, 779
Ivison, R. J., Smail, I., Papadopoulos, P. P., et al. 2010, MNRAS, 404, 198
Kennicutt, R. C. 1998, ApJ, 498, 541
Kirkpatrick, C. C., McNamara, B. R., & Cavagnolo, K. W. 2011, ApJL, 731, L23
Klamer, I. J., Ekers, R. D., Sadler, E. M., et al. 2004, ApJL, 612, L97
Kroupa, P. 2001, MNRAS, 322, 231
Lacy, M., Baum, S. A., Chandler, C. J., et al. 2020, PASP, 132, 035001
McMullin, J. P., Waters, B., Schiebel, D., Young, W., & Golap, K. 2007, ASP Conference Series 376, Astronomical Data Analysis Software and Systems XVI, ed. R. A. Shaw, F. Hill, & D. J. Bell, (San Francisco, CA: Freeman), 127
Miley, G. K., Overzier, R. A., Zirm, A. W., et al. 2006, ApJL, 650, L29
Narayanan, D., Turk, M., Feldmann, R., et al. 2015, Natur, 525, 496
Pâris, I., Petitjean, P., Ross, N. P., et al. 2017, A&A, 597, A79
Reuland, M., van Breugel, W., Röttgering, H., et al. 2003, ApJ, 592, 755
Riechers, D. A., Carilli, C. L., Maddalena, R. J., et al. 2011, ApJL, 739, L32
Rosdahl, J., & Blaizot, J. 2012, MNRAS, 423, 344
Solomon, P. M., & Vanden Bout, P. A. 2005, ARA&A, 43, 677
Vernet, J., Lehnert, M. D., De Breuck, C., et al. 2017, A&A, 602, L6
Villar-Martín, M., Vernet, J., di Serego Alighieri, S., et al. 2003, MNRAS, 346, 273
Wang, R., Carilli, C. L., Wagg, J., et al. 2008, ApJ, 687, 848